Nonlinear Wavefield Characteristics of Seismic Translation and Rotation in Small-Strain Deformation from Moment Tensor Simulations

Wei Li [1,2], Yun Wang [1,2,*], Chang Chen[1,2], Lixia Sun[1,3]

[1] *"MWMC" group, School of Geophysics and Information Technology, China University of Geosciences, Beijing 100083, China*

[2] *State Key Laboratory of Geological Processes and Mineral Resources, China University of Geosciences, Beijing 100083, China*

[3] *Sinopec Research Institute of Petroleum Engineering Co., Ltd., Beijing 102206, China*

[*] Corresponding author: wangyun@mail.gyig.ac.cn.

Abstract Seismic rotational motions recorded in near-field and strong-motion observations show discrepancies with theoretical predictions derived from linear elastodynamic theory. To investigate potential nonlinear contributions, this study incorporates geometric nonlinear effects into wave propagation theory using the Green-Lagrange strain tensor. A staggered-grid finite-difference method is used to simulate six-component (translational and rotational) wavefields generated by three basic moment-tensor source types~~fundamental seismic sources~~: isotropic (ISO), double-couple (DC), and compensated linear vector dipole (CLVD). The results demonstrate that nonlinear effects, as a secondary source, have a universal intensity pattern adhering to the physics of wave motion. However, the ~~excitation~~ efficiency of

23 exciting these effects and the modulation of wavefield attributes (such as P-wave

24 polarization) depend strongly on source type. Simulations show that rotational

25 components exhibit higher sensitivity to nonlinear effects driven by S-waves.

26 Reference simulations of two moderate-to-strong earthquakes suggest that surface

27 waves are the primary carriers of nonlinear features.

29 1 Introduction

30 Seismic rotational motion is a significant part of ground shaking, particularly

31 recordable in strong-motion events (Graizer, 1991; 2010; Zhou et al., 2019). Under

32 near-field and shallow-source conditions, these rotational motions exhibit pronounced

33 characteristics (Kozak, 2009; Sun et al., 2017) and play a critical role in the seismic

34 design and stability assessment of structures (Li, 1991; Yan, 2017; Huras et al., 2021).

35 Progress in research indicates that incorporating rotational motion data, which

36 contains information on the spatial gradients of the wavefield, can improve the

37 accuracy and stability of seismic source inversion (Bernauer et al., 2014; Donner,

38 2016; Ichinose et al., 2021; Hua and Zhang, 2022).

39 In a review of advances in rotational seismology, Lee et al. (2009) suggested

40 that the measured rotational components in strong ground motion may originate from

41 nonlinear elasticity and site effects. This suggestion is based on empirical evidence

42 from observations in Japan and Taiwan, where rotational measurements are typically

43 one to two orders of magnitude larger than those expected from classical linear

44 elasticity theory or derived from translational data, indicating the limitations of linear

45 theory. In geophysics, nonlinearity often refers to constitutive nonlinearity related to

46 material behavior, such as the hysteretic and elastoplastic responses of soils and rocks

47 under large strains (Frankel et al., 2002; Bonilla et al., 2005; Bonilla et al., 2011;

48 Frankel et al., 2002; Régnier et al., 2018). This type of nonlinearity involves intrinsic

49 energy dissipation and plastic deformation, resulting in nonlinear site amplification in

50 strong-motion records (Régnier et al., 2018).

51   On the other hand, nonlinearity can also arise from the geometric description of

52   an object's deformation itself, known as geometric nonlinearity. Even if a material

53   adheres to Hooke's law, the mathematical relationship between strain and

54   displacement can still contain higher-order nonlinear terms. This geometric

55   nonlinearity is significant when describing seismic wave propagation in pre-stressed

56   media (Tromp and Trampert, 2018). However, current research has predominantly

57   focused on material constitutive nonlinearity and its linearized approximation

58   (Renaud et al., 2012; 2013; TenCate et al., 2016; Feng et al., 2018), with a systematic

59   investigation into the strain nonlinearity introduced by the measure of deformation,

60   and its expression in seismic wave propagation, is still lacking. This neglected aspect

61   may contribute to understanding the complex rotational motions observed in the near

62   field of strong earthquakes.

63   Therefore, this study aims to systematically characterize geometric nonlinear

64   effects within the framework of the small-strain assumption by incorporating the

65   Green-Lagrange strain tensor. We employ a staggered-grid finite-difference method to

66   simulate three fundamental moment tensor sources, exploring how geometric

67   nonlinearity leads to body-wave coupling and energy redistribution, and its intrinsic

68   dependence on the source type. Furthermore, using two moderate-to-strong

69   earthquakes in the Taiwan region as examples, we explore the manifestation of

70   nonlinear effects in a more complex scenario.

71   2 Theory and method

72   2.1 Elastodynamic theory

73   Consider a three-dimensional (3D) elastic medium in an orthogonal Cartesian

74   coordinate system (Fig. 1). An infinitesimal line element connecting a particle A at

75   position **x** and an adjacent particle B at **x**+d**x** has an initial length of ds. When

76   subjected to external force, this element undergoes a displacement $\boldsymbol{u}(\boldsymbol{x}, t)$, moving to

77   new positions A' and B' at **x'** and **x'**+d**x'**, respectively, with a deformed length of ds'.

78   This process includes both rigid-body displacement and strain-induced distortion. The

79   strain energy density can be characterized by the quadratic form of the change in the

80   element's length, as shown in Eq. (1).

81
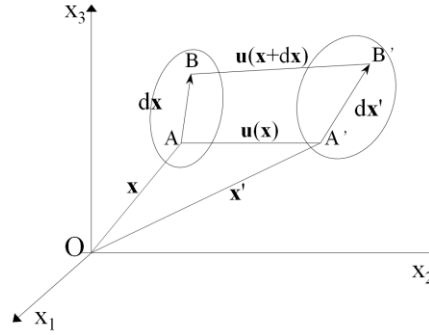
82   **Figure 1.** Schematic diagram of displacement and deformation of an infinitesimal line

83   element in an elastic medium (adapted from Aki and Richards (2002))

84    $$(ds')^2 - (ds)^2 = 2E_{ij}dx_i dx_j, \ i, j \in \{1, 2, 3\} \tag{1}$$

85   where E_{ij} is the Green-Lagrange strain tensor, which provides an objective measure of

86   deformation. In Cartesian coordinates, E_{ij} is defined by the displacement field as:

87    $$E_{ij} = \frac{1}{2}\left(\frac{\partial u_j}{\partial x_i} + \frac{\partial u_i}{\partial x_j} + \frac{\partial u_k}{\partial x_i} \cdot \frac{\partial u_k}{\partial x_j}\right), \ i, j, k \in \{1, 2, 3\} \tag{2}$$

88   The displacement gradient tensor can be decomposed into a symmetric strain

89   tensor (e_{ij}) and an antisymmetric rotation tensor (r_{ij}):

90
$$\frac{\partial u_j}{\partial x_i} = e_{ij} + r_{ij} \tag{3}$$

91 where,

92
$$e_{ij} = \frac{1}{2}(\frac{\partial u_j}{\partial x_i} + \frac{\partial u_i}{\partial x_j}), \quad r_{ij} = \frac{1}{2}(\frac{\partial u_i}{\partial x_j} - \frac{\partial u_j}{\partial x_i}) \tag{4}$$

93 Traditional linear elasticity simplifies the problem by neglecting the second-order

94 product of displacement gradients in Eq. (2), thus reducing the Green-Lagrange strain

95 tensor to the strain tensor e_{ij}:

96
$$E_{ij} \approx e_{ij} = \frac{1}{2}(\frac{\partial u_j}{\partial x_i} + \frac{\partial u_i}{\partial x_j}) \tag{5}$$

97 For an isotropic medium, the stress-strain constitutive relationship is linear

98 (generalized Hooke's law), given by Eq. (6), where λ and μ are the Lamé constants.

99
$$\sigma_{ij} = \lambda \delta_{ij} e_{kk} + 2\mu e_{ij} \tag{6}$$

100 The theoretical framework of this study consistently employs the linear

101 constitutive relationship described by Eq. (6). However, the complete Green-Lagrange

102 strain tensor E_{ij} (rather than its linear approximation e_{ij}) is substituted into it, yielding

103 a stress expression that reflects geometric nonlinearity:

104
$$\sigma_{ij} = \lambda \delta_{ij} e_{kk} + 2\mu e_{ij} + \underbrace{\frac{1}{2}\lambda \delta_{ij}(\frac{\partial u_k}{\partial x_m} \cdot \frac{\partial u_k}{\partial x_m}) + \mu \frac{\partial u_k}{\partial x_i} \cdot \frac{\partial u_k}{\partial x_j}}_{\text{additional terms}}, \quad i, j, k, m \in \{1, 2, 3\} \tag{7}$$

105 Substituting this stress expression into the momentum conservation law (Eq. (8)),

106
$$\rho \frac{\partial^2 u_i}{\partial t^2} = \frac{\partial \sigma_{ij}}{\partial x_j} \tag{8}$$

107 where ρ is the medium density, we finally obtain the nonlinear wave equation:

108
$$\rho \frac{\partial^2 u_i}{\partial t^2} = \underbrace{(\lambda + \mu) \frac{\partial^2 u_j}{\partial x_i \partial x_j} + \mu \frac{\partial^2 u_i}{\partial x_j \partial x_j}}_{\text{original terms}} + \underbrace{\lambda \frac{\partial u_k}{\partial x_i} \frac{\partial^2 u_k}{\partial x_j x_j} + \mu \left(\frac{\partial^2 u_k}{\partial x_i x_j} \frac{\partial u_k}{\partial x_j} + \frac{\partial^2 u_k}{\partial x_j x_j} \frac{\partial u_k}{\partial x_i} \right)}_{\text{additional terms}}, \ i,j,k \in \{1,2,3\} \quad (9)$$

109   In Eq. (9), under the small-strain assumption, the original terms constitute the

110   classic wave equation, while the subsequent additional terms arise from the geometric

111   nonlinearity of strain. These additional terms mathematically act as endogenous,

112   secondary body force sources that depend on the wavefield itself. In linear theory,

113   P-waves (driven by the divergence field, representing volume change) and S-waves

114   (driven by the curl field, representing shape change) are strictly decoupled. However,

115   the existence of these nonlinear terms disrupts this decoupling. Specifically, the term

116    $\partial u_k / \partial x_i \cdot \partial u_k / \partial x_j$ is a product of displacement gradients (which include both strain and

117   rotation). When the P-wave (dominated by compressional strain) propagates, its

118   non-uniform strain field generates spatial gradients. Through these higher-order terms,

119   the gradient field of the P-wave can generate an equivalent body force source with a

120   curl component within the medium, which in turn radiates S-waves. The reverse is

121   also true. This is the fundamental physical mechanism of P-S mode conversion:

122   energy is transferred between the compressional and shear modes through the

123   self-interaction of the wavefield.

124   2.2 Staggered-grid finite-difference method

125   To solve the nonlinear wave equation (9), we employ a high-accuracy

126   Staggered-Grid Finite-Difference (SGFD) method (Virieux, 1986; Sun et al., 2018).

127   First, by taking the time derivative of the nonlinear constitutive relation (7) and

128   combining it with the momentum conservation equation (8), we convert the

129   second-order wave equation into a system of first-order velocity-stress partial

130   differential equations. This system includes additional stress-rate terms generated by

131   the second-order products of displacement gradients. These terms update the

132   displacement field through time integration of the velocity field, thereby

133   implementing the nonlinear coupling. The resulting velocity-stress equations are:

134
$$\begin{cases} \rho \dfrac{\partial v_i}{\partial t} = \dfrac{\partial \sigma_{ij}}{\partial x_j} \\ \dfrac{\partial \sigma_{ij}}{\partial t} = \lambda \delta_{ij} \dfrac{\partial E_{kk}}{\partial t} + 2\mu \dfrac{\partial E_{ij}}{\partial t} \\ \qquad = \lambda \delta_{ij} \dfrac{\partial v_k}{\partial x_k} + \mu(\dfrac{\partial v_i}{\partial x_j} + \dfrac{\partial v_j}{\partial x_i}) + \underbrace{\lambda \delta_{ij}(\dfrac{\partial v_k}{\partial x_m} \cdot \dfrac{\partial u_k}{\partial x_m}) + 2\mu \dfrac{\partial v_k}{\partial x_i} \cdot \dfrac{\partial u_k}{\partial x_j}}_{\text{additional terms}} \end{cases}, \; i, j, k, m \in \{x, y, z\} \quad (10)$$

135   where $v_i = \partial u_i / \partial t$. In the SGFD scheme, different physical quantities are staggered

136   on the spatial grid cells. This arrangement naturally satisfies the central-difference

137   approximation for differential operators, effectively suppressing numerical dispersion

138   and enhancing computational stability and accuracy, as illustrated in Fig. 2.

139
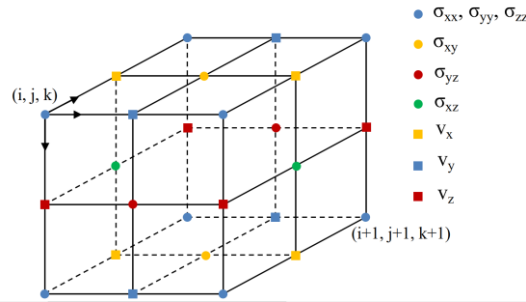
140   **Figure 2.** 3D staggered-grid configuration for velocity-stress formulations,

141   showing the placement of velocity components and stress components.

142   To handle the model's truncated boundaries, we employ the Perfectly Matched

143   Layer (PML) absorbing boundary condition (Li et al., 2015). For simulations

144   involving a free surface, the free boundary is implemented at the top of the model by

145   setting the acoustic boundary replacement (Xu et al., 2007; Wang et al., 2012). The

146   numerical code used in this study has been benchmarked against international

147   standard programs, ~~including~~ using SPICE/SISMOWINE ~~and SPECFEM2D~~. The

148   comparison is provided in the supplementary material.

149   2.3 Source implementation and simulation parameters

150   The seismic moment tensor M_{ij} is the complete representation of an equivalent

151   body-force system for a point source (Gilbert, 1970). It can be decomposed into three

152   fundamental components: isotropy (ISO), double couple (DC), and compensated

153   linear vector dipole (CLVD) (Knopoff and Randall, 1970; Jost and Hermann, 1989).

154   These moment tensor expressions can be written as Eq. (11).

$$
\boldsymbol{M}^{ISO} = \begin{pmatrix} M_{xx} & 0 & 0 \\ 0 & M_{yy} & 0 \\ 0 & 0 & M_{zz} \end{pmatrix}, \boldsymbol{M}^{DC} = \begin{pmatrix} 0 & M_{xy} & 0 \\ M_{yx} & 0 & 0 \\ 0 & 0 & 0 \end{pmatrix}, \boldsymbol{M}^{CLVD} = \begin{pmatrix} M_{xx} & 0 & 0 \\ 0 & M_{yy} & 0 \\ 0 & 0 & -2M_{zz} \end{pmatrix} \tag{11}
$$

156   In our SGFD framework, we follow the method proposed by Graves (1996) to

157   implement the moment tensor source by converting the moment rate tensor into

158   equivalent body forces. The equivalent velocity increment Δv^n added on the grid can

159   be expressed as:

$$
\boldsymbol{M}^{ISO}: \Delta v_i^n = \frac{M_{ij} \cdot dt \cdot f^n}{\rho V} \cdot \frac{\partial}{\partial x_j}
$$

$$
\boldsymbol{M}^{DC}: \Delta v_i^n = \frac{M_{jk} \cdot dt \cdot f^n}{\rho V} \cdot (\delta_{ij} \frac{\partial}{\partial x_k} + \delta_{ik} \frac{\partial}{\partial x_j}) \tag{12}
$$

$$
\boldsymbol{M}^{CLVD}: \Delta v_i^n = \frac{M_{kl} \cdot dt \cdot f^n}{\rho V} \cdot (\delta_{ik} \frac{\partial}{\partial x_l} + \delta_{il} \frac{\partial}{\partial x_k} - \frac{2}{3} \delta_{kl} \frac{\partial}{\partial x_i})
$$

161   where $i, j, k, l \in \{x, y, z\}$. Δv is the velocity increment, n is the time-step index, dt is

162   the time step, ρ is the density, V is the grid cell volume, and f^n is the value of the

163   source-time function at time n dt.

164   We conduct simulations in a homogeneous, isotropic, 3D full-space model to

165   isolate the effects of nonlinearity from those of complex media. The model parameters

166   are: P-wave velocity v_p=4400 m/s, S-wave velocity v_s=3000 m/s, and density ρ=2600

167   kg/m^3. The model space is 14 km $\times$ 14 km $\times$ 14 km, with a uniform grid spacing of Δx

168   = Δy = Δz = 50 m. The source is located at the model center. It uses a Ricker wavelet

169   with a dominant frequency of 4 Hz as the source-time function. Receivers are

170   arranged on a spherical surface with a radius of 5 km centered at the source to sample

171   wavefields at various azimuths. The time step is $\Delta t = 0.0015$s.

172   The shortest wavelength for the 4 Hz dominant frequency is the S-wavelength

173   ($\lambda_S = 750$ m). Based on the 50 m grid spacing, there are 15 grid points per wavelength,

174   which is well above the threshold required for high-order finite-difference schemes

175   (Virieux, 1986). The Courant-Friedrichs-Lewy (CFL) number is approximately 0.23,

176   which is well below the stability limit for 3D finite-difference methods (Moczo et al.,

177   2007), ensuring the stability and accuracy of the numerical computation.

178   3 Comparison of simulation results

179   3.1 Basic characteristics of nonlinear seismic wavefields

180   Fig. 3(a) displays the 6C wavefield snapshots for the ISO source at t=1.5s, while

181   Fig. 3(b) compares the linear and nonlinear waveforms recorded at a specific receiver.

182   Within the framework of linear theory, an ISO source only generates P-waves in

183   homogeneous elastic media. However, a faint signal is still recorded in the P-wave

184   window of the rotational components in the linear simulation (black line). This signal

185 originates from the spatial gradients produced by the wavefront curvature of the

186 near-field P-wave. In the far field, P-wave~~a~~ can be approximated as an irrotational

187 plane wave with no curl in its displacement field. In the near field, however, the

188 spatial gradients of its displacement field can generate weak rotation. This signal is

189 very weak compared to the rotational signals generated by S-waves, and is therefore

190 treated in this study as the baseline background for assessing the nonlinear

191 contributions.

192   The waveform comparison shows that in the S-wave window, the nonlinear

193 simulation exhibits a distinct response with obvious amplitude, whereas the linear

194 simulation is near zero in the ISO results. This vibration is attributed to the P-to-S

195 mode conversion of energy, caused by geometric nonlinearity. Analysis of the

196 waveform characteristics in Fig. 3(b) reveals that the EM caused by nonlinearity is

197 larger in the rotational components than in the translational ones, while the PM is

198 nearly zero. This indicates that the primary effect of geometric nonlinearity is to

199 modulate the energy distribution and envelope shape of the waves, rather than

200 perturbing their _fundamental_ propagation ~~velocity or arrival time~~ phase. This effect

201 originates from the higher-order nonlinear terms in the strain-displacement

202 relationship. These terms act as new, endogenous body force terms in the wave

203 equation, equivalent to producing minor secondary perturbations in the wave's

204 propagation. These perturbations interact with the primary wavefield, thereby

205 reallocating energy and ultimately altering the wave's amplitude and shape. For

206 instance, as a P-wave from an ISO source propagates, its non-uniform strain field

207   generates spatial gradients. Through the self-interaction of these gradients via the

208   nonlinear terms, an equivalent body force source with a curl component is generated

209   within the medium, which then radiates S-waves.

210

211
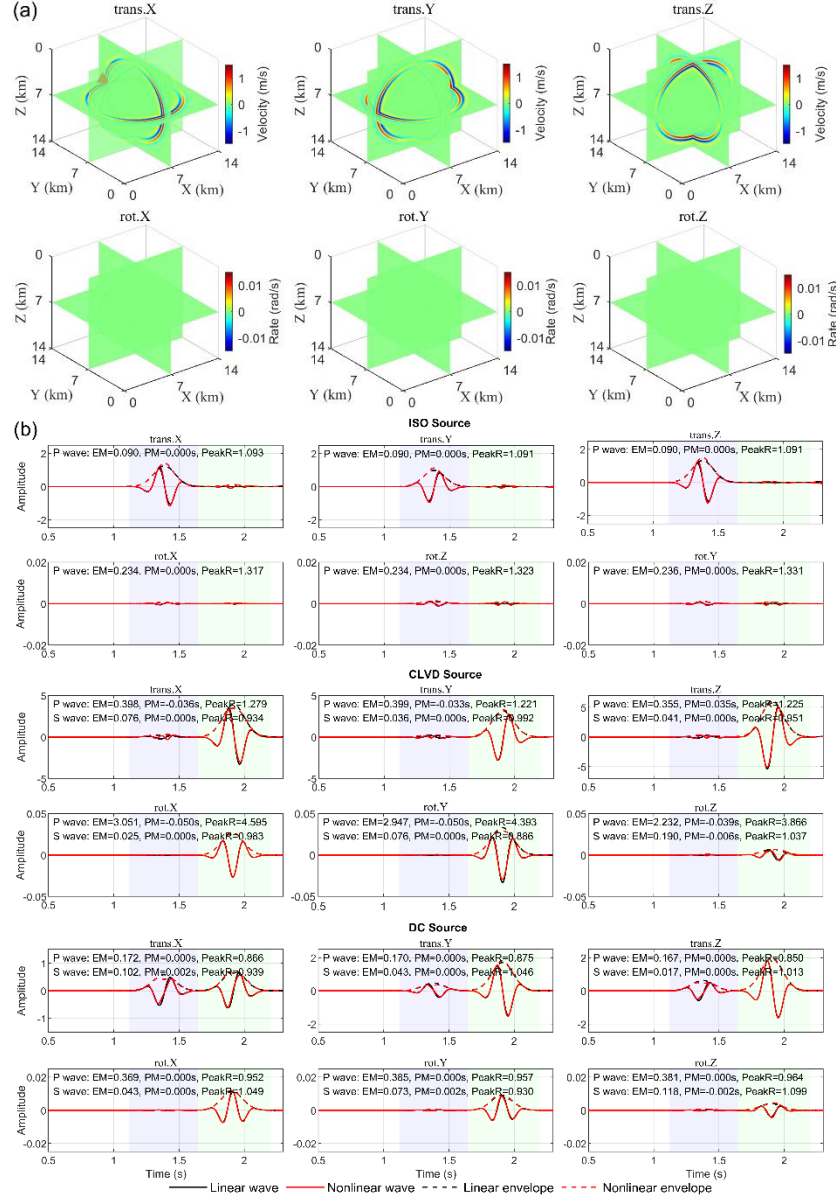
212   **Figure 3.** (a) Snapshot of the 6C wavefield from the linear ISO source simulation and

213   the location of the example receiver (indicated by the red triangle on the trans.X

214   component). (b) Comparison of the waveforms and envelope characteristics of the

215   linear and nonlinear simulations at this receiver. The P-wave and S-wave analysis

216   windows are marked. EM: envelope misfit; PM: phase misfit; PeakR: Peak ratio.

217

218   We next calculated the energy of the residual waveforms between the linear and

219   nonlinear simulations. Fig. 4 shows the projection of this metric in the P-wave and

220   S-wave windows onto three principal planes.

221

222
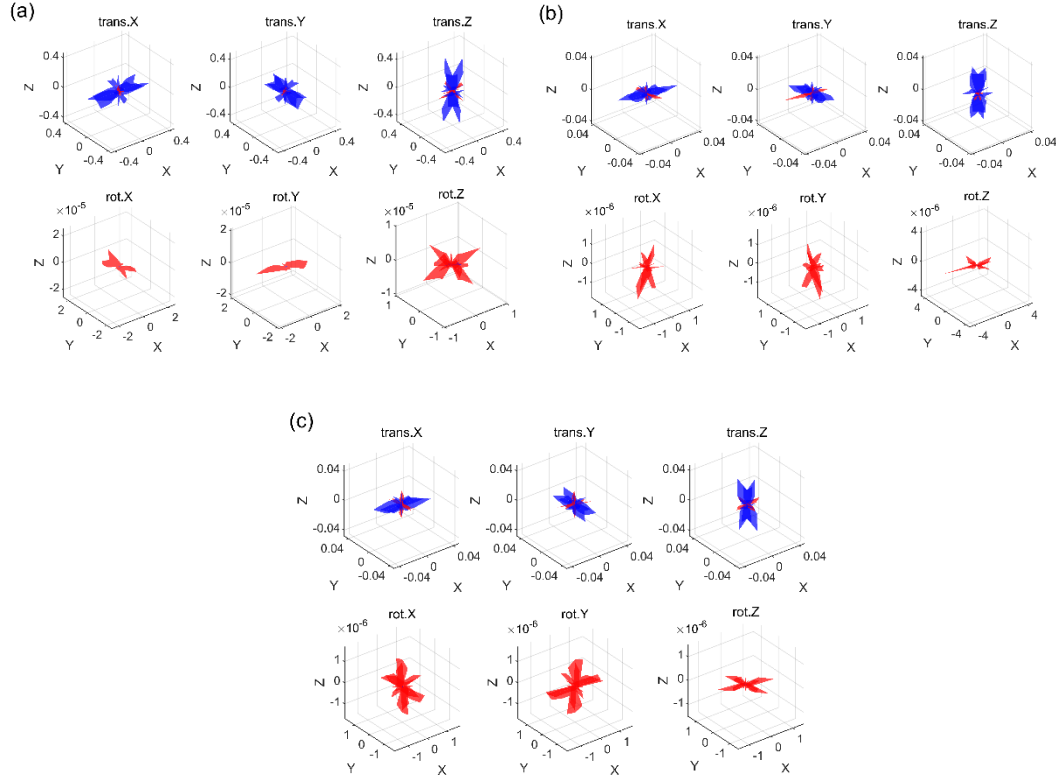
223   **Figure 4.** 3D spatial projection of the intensity of waveform perturbations

224   generated by nonlinearity. (a)-(c) are the results for CLVD, DC, and ISO sources,

225   respectively. Each subplot shows the projection of the nonlinear effect intensity of the

226   P-wave (blue) and the S-wave (red).

227   The results indicate that the radiation of the nonlinear effect follows fundamental

228   wave physics principles. In the translational components, the nonlinear effect of the

229   P-wave is much stronger than that of the S-wave, and its dominant direction is

230   consistent with the corresponding coordinate axes, reflecting the direction of the

231   strongest strain gradient in the linear P-wave field. Consequently, the nonlinear effect

232   is strongest in the direction where the theoretical linear P-wave amplitude projects

233   most strongly onto the corresponding Cartesian component (e.g., the X-axis direction

234   for the trans.X component). In the rotational components, the nonlinear perturbation

235   in the S-wave is dominant. This is because rotational motion is generated by shear

236   strain gradients, and the S-wave, carrying substantial shear energy, is most effective at

237   producing the shear strain gradients required to drive rotation.

238   Building on the time-domain analysis, spectral analysis was conducted on

239   waveforms in the P- and S-wave windows of the median and interquartile range (IQR)

240   of the Power Spectral Density (PSD), as shown in Fig. 5. For the CLVD and DC

241   sources, the median nonlinear spectrum is systematically higher than the median

242   linear spectrum in the mid-to-high frequency band (approx. 5-20 Hz) in both P- and

243   S-waves, and this phenomenon is more pronounced in the rotational components. The

244   translational component spectra are nearly identical in the ISO source simulation. In

245   the S-wave comparison for the ISO source, the linear translational and rotational

246   energies are extremely low, essentially at the level of numerical simulation noise. In

247   contrast, the nonlinear spectrum is several orders of magnitude higher, providing

248   frequency-domain evidence for the nonlinear P-S mode conversion. The IQR of the

249   PSD indicates that the nonlinear effects exhibit strong spatial variability, being

250   enhanced in some azimuths while potentially being weakened in others, thus showing

251   significant azimuthal dependence. The spectral comparison reveals a key feature of

252   the nonlinear effect: energy transfer to higher frequencies. The energy injected by the

253   source, primarily concentrated at lower frequencies, is efficiently pumped by the

254   nonlinear secondary source and re-radiated as higher-frequency energy. This

255   redistribution of high-frequency energy, accompanied by the mode conversion of P-

256   and S-waves, collectively causes the nonlinear spectral lines to be systematically

257   higher than the linear ones in the mid-to-high frequency range.

258
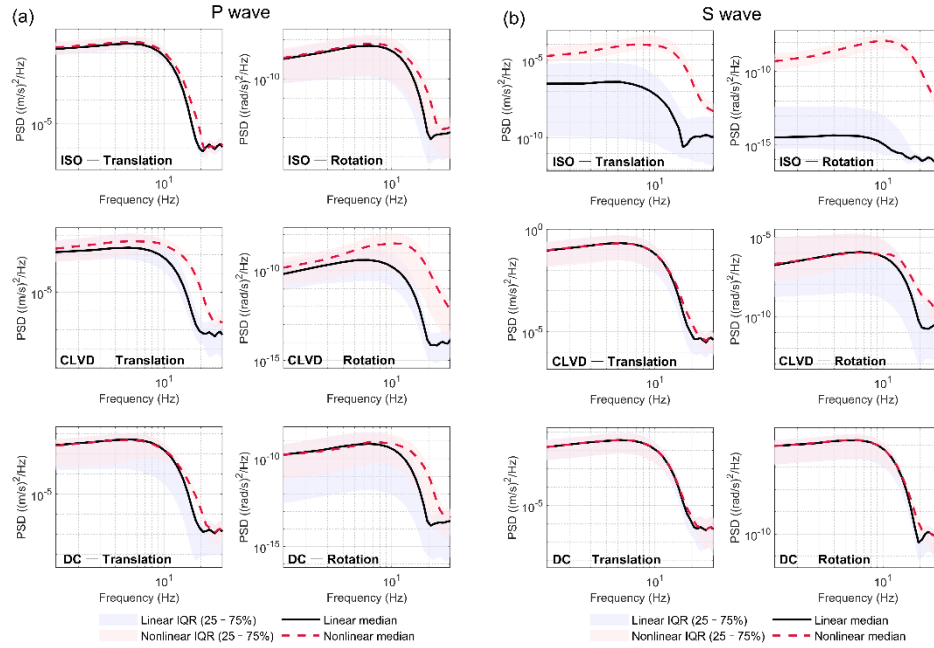
259   **Figure 5.** Comparison of the (a) P-wave and (b) S-wave PSD of translational and

260   rotational components. The black solid line is the median PSD from the linear

261   simulations, the red dashed line is from the nonlinear simulations, and the shaded area

262   represents the 25%-75% IQR.

263   3.1 Source-type dependency of nonlinear effects

264   Fig. 6 presents the log-ratio of nonlinear to linear energy ($\log(E_{nl} / E_{lin})$) for the

265   tangential energy in the P-wave (E^P) and the radial energy in the S-wave (E^S). The

266   energy E is obtained by time-integrating the square of the wavefield amplitude. Fig. 6,

267   through scatter plots and statistics, shows the distribution of the logarithmic energy

268 ratios for the three source types, quantitatively assessing the overall impact of

269 nonlinear effects on the energy of specific wave types.

270   Regarding the tangential energy in the P-wave (Fig. 6(a)), the nonlinear

271 enhancement is most significant for the CLVD source, followed by the DC source,

272 while the effect of the ISO source is minimal. This indicates that the CLVD source is

273 the most effective mechanism for exciting the nonlinear growth of P-wave tangential

274 energy. For the radial energy in the S-wave (Fig. 6(b)), the net effect of nonlinearity

275 for the CLVD and DC sources is not statistically significant, possibly due to the

276 cancellation of azimuthal enhancement and reduction.

277
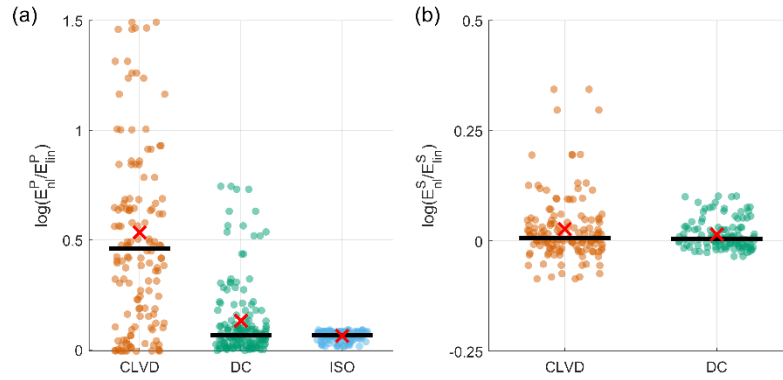
278   **Figure 6.** Distribution of the nonlinear/linear log-ratio for (a) tangential energy

279   in the P-wave and (b) radial energy in the S-wave. The dots represent the values for

280   each independent receiver; the black bar indicates the median of the data; the red

281   cross indicates the arithmetic mean.

282   To further investigate the impact of nonlinearity on the micro-properties of the

283 wavefield, we introduce two quantitative metrics to analyze the waveform attribute

284 changes within the P-wave window. First, we use rectilinearity (rect) to measure the

285 deviation of P-wave particle motion from a straight line. This metric is calculated

286 based on the eigenvalues $(\lambda_1 \geq \lambda_2 \geq \lambda_3)$ of the covariance matrix of the

287 three-component particle motion data. While commonly defined as $1 - (\lambda_2 + \lambda_3) / 2\lambda_1$

288 (Jurkevics, 1988), we use a simplified and sensitive form, $rect = (\lambda_1 - \lambda_2) / \lambda_1$. In this

289 formulation, a value approaching 1 indicates purely unidirectional motion, whereas a

290 value close to 0 indicates circular or random motion. The sign of the change, $\Delta rect =$

291 $rect_{nl} - rect_{lin}$, reflects whether the nonlinearity promotes or suppresses the leakage of

292 P-wave energy into the tangential direction. Second, to explore the coupling

293 relationship between different motion modes, we introduce the rotation-translation

294 correlation (corr). This metric ~~calculates~~ is the Spearman's rank correlation coefficient

295 between the time series of the tangential velocity magnitude and the rotation rate

296 magnitude~~,~~. This non-parametric metric was chosen to robustly quantify~~ing~~ the

297 synchrony of the time-varying intensity envelopes ~~of these two physical motions~~. It

298 effectively assesses whether the two intensities trend together (i.e., a monotonic

299 relationship), regardless of the specific functional form linking them (Press et al.,

300 1986).

301   Fig. 7(a) shows the statistical distribution of the differences in these two metrics.

302 For all three sources, $\Delta corr$ is generally positive, indicating that geometric

303 nonlinearity may be a common physical mechanism that enhances the coupling

304 between rotation and translation. In contrast, the distribution of $\Delta rect$ shows a

305 pronounced source dependence: the ISO source causes weak changes, the DC source

306 induces significant negative changes, while the CLVD source primarily causes

307 positive changes. The spatial distribution of $\Delta rect$ in Fig. 7(b) further reveals its

308   essential connection to the source's strain state. For the ISO source, characterized by

309   pure volumetric strain, the pure volumetric strain excites a very weak shear effect

310   through nonlinearity, leading to a slight decrease in P-wave rectilinearity, but the

311   efficiency of this conversion is extremely low. For the pure-shear DC source, the

312   significant decrease in rectilinearity is concentrated near the P-wave radiation nodes,

313   which are the regions with the strongest linear shear strain gradients. This indicates

314   that in these regions, the efficiency of the nonlinear P-S mode conversion is highest,

315   leading to a noticeable decrease in rectilinearity. For the CLVD source, which

316   combines strong uniaxial compression and axisymmetric shear, the increase in

317   rectilinearity is also concentrated in regions with strong strain gradients. The result

318   reveals that, in a complex stress state with coexisting tension and compression, the

319   nonlinear effect may instead constrain energy to propagate in the radial direction,

320   suppressing leakage into the tangential direction, thereby purifying the P-wave

321   motion.
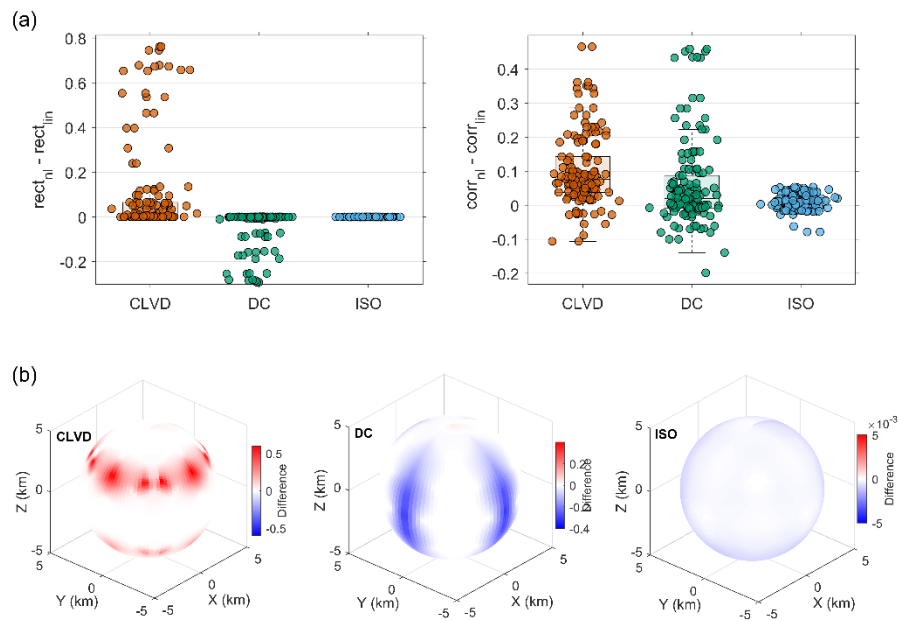
324   **Figure 7.** (a) Statistical distribution of the change in P-wave rectilinearity and

325   rotation-translation correlation changes, and (b) spherical spatial distribution of Δrect

326   in different receivers.

327   In summary, the analysis of the wavefield properties demonstrates that the

328   manifestation of nonlinear effects is fundamentally controlled by the type of strain

329   field initialized by the source and the geometry of its spatial gradients. Different

330   source mechanisms, by initializing different strain fields, thus modulate the mode,

331   intensity, and even the effect of the nonlinear response.

332   4 Simulation of nonlinear effects for referenced earthquake events

333   To extend the understanding established in the idealized full-space model to

334   more realistic scenarios involving complex propagation effects, we further simulate

335   two moderate-to-strong referenced earthquakes that occurred in the coastal region of

336   Taiwan: event E1 (Mw 5.4) and event E2 (Mw_6.1). The epicenters and station

337   locations of these two referenced events are shown in Fig. S34. Unlike the preceding

338   basic source simulations, the models in this section employ a layered velocity

339   structure based on the CRUST1.0 model (Laske et al., 2013) to approximate the real

340   Earth's structure (see Table S45). The source mechanisms for both events (Eq. (13))

341   are composite, containing both non-double-couple and double-couple

342   componentsmixed sources. Other detailed simulation parameters for the two

343   referenced earthquake simulations are provided in Table S56.

$$E1: \begin{bmatrix} M_{xx} = -7.569 \times 10^{16}, M_{yy} = -2.373 \times 10^{16}, M_{zz} = 9.942 \times 10^{16} \\ M_{xz} = 7.372 \times 10^{16}, M_{yz} = -1.0965 \times 10^{17}, M_{xy} = 4.156 \times 10^{16} \end{bmatrix}$$

$$E2: \begin{bmatrix} M_{xx} = -1.064 \times 10^{18}, M_{yy} = -7.607 \times 10^{17}, M_{zz} = 1.8247 \times 10^{18} \\ M_{xz} = 3.141 \times 10^{17}, M_{yz} = 3.155 \times 10^{17}, M_{xy} = 1.114 \times 10^{18} \end{bmatrix}$$

(13)

Fig. 8 shows the results for the E1. Compare the waveforms and the time-frequency spectral ~~energy~~ differences, where the spectra are calculated using a Generalized S-Transform (GST) (Stockwell, 1996), as shown in Fig. 8(b). These differences are defined as the spectra of the nonlinear simulations minus those of the linear simulations. In the translational components, the energy changes induced by nonlinearity are relatively dispersed in different types of waves. However, most are concentrated during the arrival of S-wave (approx. 15-20 s) and the subsequent surface waves, and faint but persistent nonlinear perturbations are also observed during the P-wave and its subsequent multiple reflections/conversions (approx. 5-15 s). In the rotational components, the nonlinear response energy is more concentrated than in the translational components. Energy perturbations can be observed on the rot.T component before the direct S-wave arrival, which may correspond to nonlinear effects excited by S-waves converted from P-waves or S-waves reflected/transmitted within the layered medium. For the rot.R and rot.Z components, the nonlinear effects are primarily associated with the arrival of the direct S-wave. Different components showing different extents of nonlinearity may stem from the azimuthal location of this receiver.
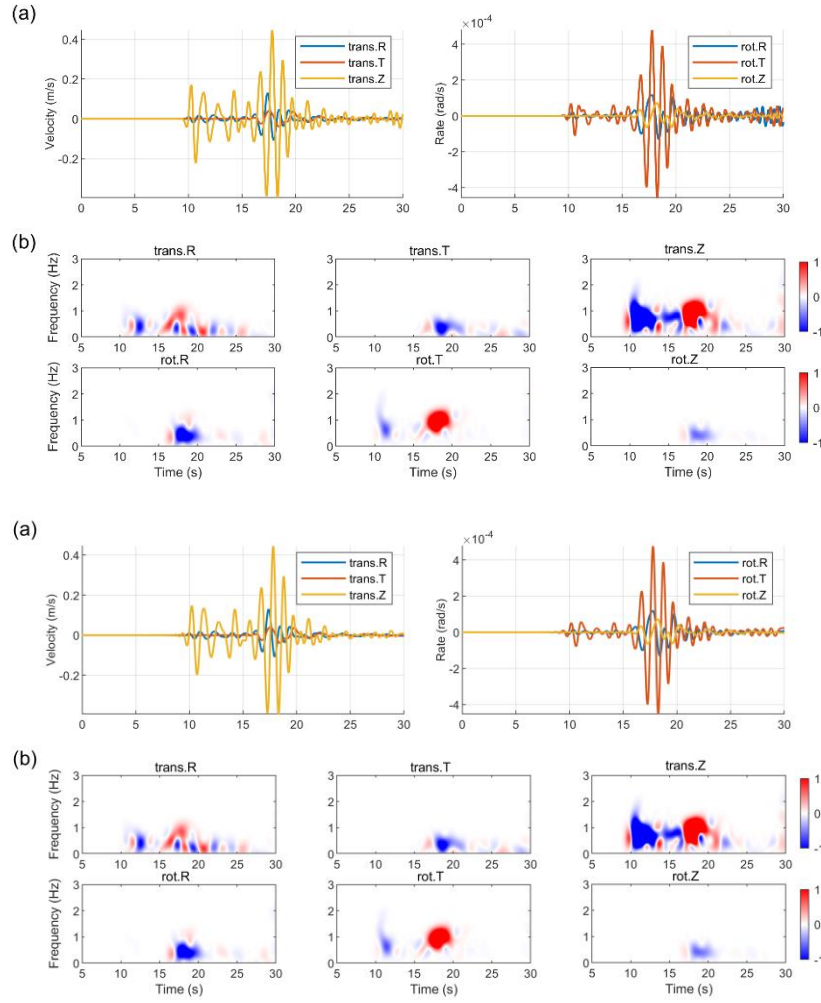
Figure 8. (a) Synthetic linear 6C waveforms (low-pass filtered at 2 Hz) and (b) normalized time-frequency ~~energy~~ spectral differences (the nonlinear minus the linear) for event E1.

Numerical simulations of the E2 (Fig.9) also show nonlinear effects. Combining the time-domain waveforms (Fig. 9(a)) and the time-frequency spectral energy difference plots (Fig. 9(b)), it can be seen that significant energy changes occur in all components during the arrival of the direct S-wave (approx. 90 s) and the strong surface waves. A long-duration, very-low-frequency (<0.2 Hz) energy enhancement band appears in the translational components, starting from the surface waves and continuing. This may correspond to long-period perturbations induced by strong

374   surface waves through nonlinear mechanisms, potentially involving P-S coupling in

375   layered media, while the rotational components, as displacement gradients, are not

376   sensitive to it.
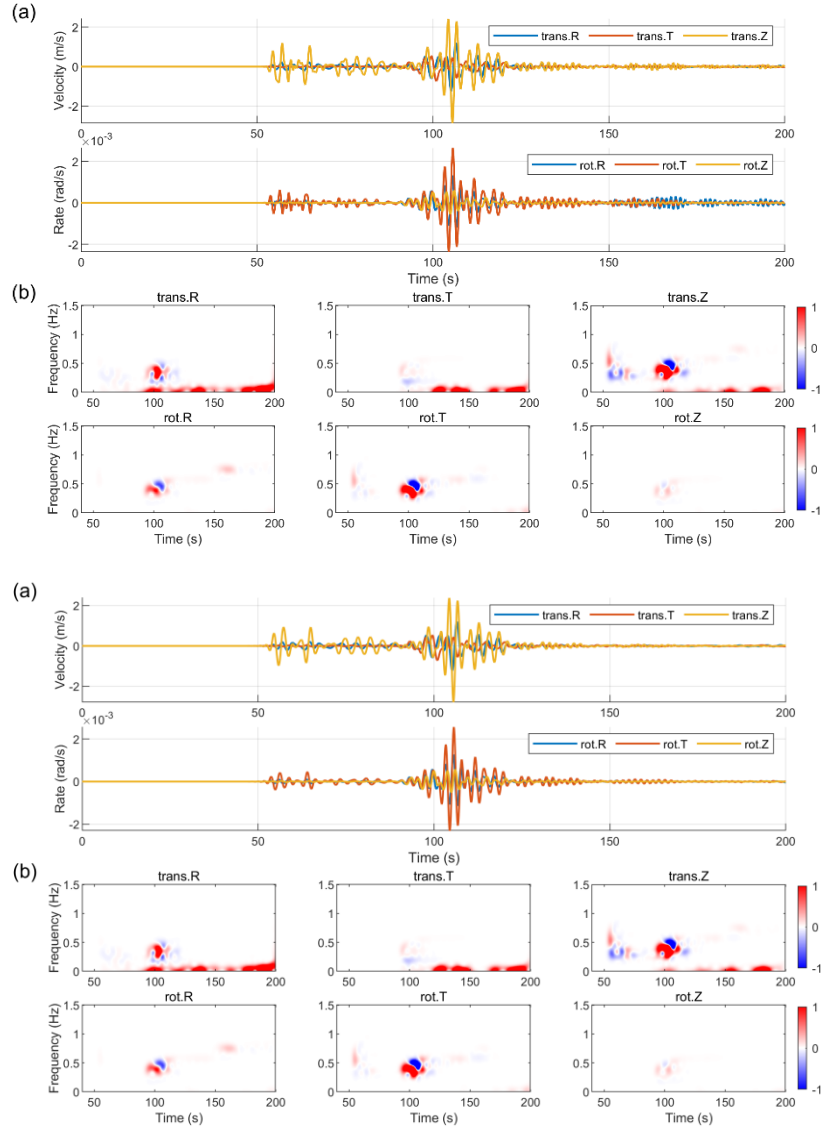
Figure 9. (a) Synthetic linear 6C waveforms (low-pass filtered at 1 Hz) and (b)

normalized time-frequency spectral ~~energy~~ differences (the nonlinear minus the linear)

for event E2.

By comparing the simulations of the two events, we find that the surface waves

are the primary phases that accumulate and carry nonlinear information. At the same

384   time, the E2 event, with its different source mechanism and further propagation path,

385   exhibits a long-period perturbation not seen in the E1 simulation. This suggests that in

386   more realistic scenarios, the physical mechanisms of nonlinear effects may be more

387   complex and can be influenced by many factors. The different nonlinear

388   characteristics displayed by the two event simulations may also be influenced by the

389   combined effects of their complex, ~~mixed~~ composite source mechanisms and the

390   specific source-station azimuth.

391   5 Discussion

392   This study, through systematic simulations of three basic moment-tensor source

393   types~~fundamental seismic sources~~ and referenced earthquake events, has

394   demonstrated several characteristics of geometric nonlinearity in seismic wavefields.

395   First, it demonstrates that the excitation and manifestation of nonlinear effects are

396   controlled by the strain state of the linear wavefield and its spatial gradients. As

397   predicted by nonlinear elastodynamic theory, geometric nonlinearity acts as an

398   equivalent secondary source term in the wave equation, with its strength being

399   proportional to the quadratic terms of the linear strain field. The radiation of nonlinear

400   effects strictly follows the physical nature of longitudinal and transverse waves. For

401   instance, the nonlinear perturbation generated by the strain gradients of a linear

402   P-wave radiates most strongly along the principal direction of the P-wave, whereas

403   the nonlinear rotational effect generated by the shear-strain gradients of an S-wave is

404   most pronounced in regions of maximum S-wave energy. In addition, different source

405   mechanisms (volumetric, pure shear, axisymmetric shear) modulate the mode,

406   strength, and even the effect of the nonlinear response by initializing different

407   geometries of the strain field.

408   Second, rotational motion is a sensitive indicator for detecting near-field

409   nonlinear effects driven by S-waves. This stems from the physical nature of

410   rotation—it is the spatial gradient of the displacement field and is therefore more

411   sensitive to the secondary source terms driven by strain gradients. This suggests that

412   the deployment and analysis of six-component seismic data are of irreplaceable value

413   for identifying and quantifying nonlinear geophysical processes in future

414   observational studies.

415   Finally, the simulations of referenced earthquake events show that surface waves,

416   which are more concentrated in energy and have longer propagation paths, are the

417   primary carriers for accumulating and preserving nonlinear information, thus pointing

418   to a key focus for future observational data analysis. More importantly, in the stronger

419   E2 event, we observed a long-period perturbation not seen in the idealized models.

420   This phenomenon suggests that under realistic strong ground motion conditions, the

421   physical mechanisms of nonlinear effects may be more complex and diverse,

422   potentially involving deeper physical processes such as stress-induced anisotropy.

423   Limitations of this study, such as the use of idealized models, highlight the need for

424   validation with real seismic records. These indicate a direction for future research:

425   how to reliably separate and identify these unique nonlinear signals from collected

426   real seismic records, which is a mixture of complex source effects, 3D heterogeneous

427   propagation effects, and local site responses.

428   6 Conclusions

429   By incorporating geometric nonlinearity based on the Green-Lagrange strain

430   tensor, this study has conducted 6C seismic wavefield simulations for three

431   fundamental moment tensor sources and two referenced moderate-to-strong

432   earthquakes. The research aims to investigate the characteristics of near-field

433   nonlinear effects and their dependence on source mechanisms. The main conclusions

434   are as follows:

435   (i) Universal radiation pattern of the nonlinear secondary source and

436   source-dependent ~~excitation~~ efficiency of exciting the effects. On one hand, the

437   radiation pattern of nonlinearity is universal, strictly adhering to the physics of wave

438   motion: the nonlinear perturbation generated by P-wave strain gradients radiates

439   primarily along the axial direction (a longitudinal characteristic), while the

440   perturbation from S-wave shear-strain gradients radiates mainly in the orthogonal

441   plane directions (a transverse characteristic). This pattern is independent of the initial

442   force source type. On the other hand, the overall efficiency of exciting these nonlinear

443   secondary sources exhibits a strong source-type dependency. Simulation results show

444   that sources with significant shear components, such as CLVD and DC sources, are

445   far more efficient in exciting nonlinear effects than the purely volumetric ISO source.

446   (ii) High sensitivity of rotational motion to S-wave-driven nonlinearity. This is

447   primarily because rotational motion directly responds to shear-strain gradients, and

448   S-waves are the primary carriers of shear energy. Consequently, rotational motion

449   becomes an ideal window for detecting the secondary sources excited by S-waves,

450 with its nonlinear response being more pronounced than that of translational

451 components.

452   (iii) Effects of wave type and strain level. The strength of nonlinear effects is

453 correlated with the strain level (which can be approximately related to the moment

454 magnitude). More importantly, surface waves, which have more concentrated

455 energy and longer propagation paths, are more effective carriers of nonlinear

456 information than body waves. In the strong-motion event simulation, long-period

457 perturbations, possibly induced by nonlinearity, were also observed. This may

458 correspond to long-period perturbations induced by strong surface waves through

459 nonlinear mechanisms, potentially involving P-S coupling in layered media.

460

461 **Author contributions.** WL: conceptualization, methodology, investigation, formal

462 analysis, writing - original draft. YW: conceptualization, writing - original draft and

463 revised draft. CC: investigation, formal analysis. LS: methodology.

464

465 **Data availability.** All data is simulated and available upon reasonable request.

466

467 **Competing interests.** The contact author has declared that neither of the authors has

468 any competing interests.

469

470 **Disclaimer.** Publisher's note: Copernicus Publications remains neutral with regard to

471 jurisdictional claims made in the text, published maps, institutional affiliations, or any

472   other geographical representation in this paper.

473

474   **Financial support.** This research is financially supported by the National Natural

475   Science Foundation of China (No. 42150201、No. 62127815、No. U1839208).

476

477   **Acknowledgements.** We are grateful to the handling editor and anonymous reviewers

478   for their time and feedback, which have greatly improved the quality of this

479   manuscript.

480

481   References

482   Aki, K., and P. G. Richards. Quantitative seismology, 2nd ed, California: University

483   Science Books, https://doi.org/10.1029/2003EO210008, 2002.

484   Bernauer, M., Fichtner, A., and Igel, H.: Reducing nonuniqueness in finite source

485   inversion using rotational ground motions, J. Geophys. Res.-Solid Earth, 119(6),

486   4860-4875, https://doi.org/10.1002/2014JB011042, 2014.

487   Bonilla, L. F., Archuleta, R. J., and Lavallée, D.: Hysteretic and dilatant behavior of

488   cohesionless soils and their effects on nonlinear site response: Field data

489   observations and modeling. Bull. Seismol. Soc. Am., 95(6), 2373-2395.

490   https://doi.org/10.1785/0120040138, 2005.

491   Bonilla, L. F., Tsuda, K., Pulido, N., Régnier, J., and Laurendeau, A.: Nonlinear site

492   response evidence of K-NET and KiK-net records from the 2011 off the Pacific

493   coast of Tohoku Earthquake. Earth, Planets and Space, 63(7), 785-789.

494   https://doi.org/10.5047/eps.2011.06.012, 2011.

495   Donner, S., Bernauer, M., and Igel, H.: Inversion for seismic moment tensors

496   combining translational and rotational ground motions, Geophys. J. Int., 207(1),

497   562-570, https://doi.org/10.1093/gji/ggw298, 2016.

498   Feng, X., Fehler, M., Brown, S., Szabo, T. L., and Burns, D.: Short-period nonlinear

499   viscoelastic memory of rocks revealed by copropagating longitudinal acoustic

500   waves,   J.   Geophys.   Res.-Solid   Earth,   123(5),   3993–4006,

501   https://doi.org/10.1029/2017JB015012, 2018.

502   Frankel, A. D., Carver, D. L., and Williams, R. A.: Nonlinear and linear site response

503   and basin effects in Seattle for the M 6.8 Nisqually, Washington, earthquake.

504   Bull. Seismol. Soc. Am., 92(6), 2090-2109. https://doi.org/10.1785/0120000738,

505   2002.

506   Graizer, V. M.: Strong motion recordings and residual displacements: what are we

507   actually recording in strong motion seismology? Seismol. Res. Lett., 8(4),

508   635-639, https://doi.org/10.1785/gssrl.81.4.635, 2010.

509   Graizer, V. M.: Inertial seismometry methods, Earth Physics, 27(1), 51-61, 1991.

510   Graves, R. W.: Simulating seismic wave propagation in 3D elastic media using

511   staggered-grid finite differences, Bull. Seismol. Soc. Am., 86(4), 1091-1106,

512   1996.

513   Gilbert, F.: Excitation of the normal modes of the Earth by earthquake sources,

514   Geophys.   J.   R.   astr.   Soc,   22(2),   223-226,

515   https://doi.org/10.1111/j.1365-246X.1971.tb03593.x, 1970.

Hua, S. B., and Zhang, Y.: Numerical experiments of moment tensor inversion with rotational ground motions, Chinese J. Geophys., 65(1), 197-213, https://doi.org/10.6038/cjg2022P0668, 2022 (in Chinese).

Huras, L., Zembaty, Z., Bonkowski, P. A., and Bobraet, P.: Quantifying local stiffness loss in beams using rotation rate sensors, Mech. Syst. Signal Proc., 151, 107396, https://doi.org/10.1016/j.ymssp.2020.107396, 2021.

Ichinose, G. A., Ford, S. R., and Mellors, R. J.: Regional moment tensor inversion using rotational observations, J. Geophys. Res.-Solid Earth, 126(2), e2020JB020827, https://doi.org/10.1029/2020JB020827, 2021.

Jost, M. L., and Hermann, R. B.: A students guide to and review of moment tensors, Seism. Res. Lett., 60, 37-57, https://doi.org/10.1785/gssrl.60.2.37, 1989.

Jurkevics, A.: Polarization analysis of three-component array data, Bull. Seismol. Soc. Am., 78 (5), 1725–1743, https://doi.org/10.1785/BSSA0780051725,1988.

Knopoff, L., and Randall M. J.: The compensated linear-vector dipole: A possible mechanism for deep earthquakes, J. Geophys. Res., 75(26), 4957–4963, https://doi.org/10.1029/JB075i026p04957, 1970.

Kozak, J. T.: Tutorial on earthquake rotational effects: historical examples, Bull. Seismol. Soc. Am., 99(2B), 998-1010, https://doi.org/10.1785/0120080308, 2009.

Laske, G., Masters, G., Ma, Z. T., and Pasyanos, M.: Update on CRUST1. 0-A 1-degree global model of Earth's crust, EGU General Assembly 2013, 15, EGU2013-2658, 2013.

538   Lee, W. H. K., Igel, H., Todorovska, M. I., and Trifunac, M. D.: Recent advances in

539   rotational seismology, Seismol. Res. Lett., 80(3), 479–490,

540   https://doi.org/10.1785/gssrl.80.3.479, 2009.

541   Li, H. N.: Study on rotational components of ground motion, Journal of Shenyang

542   Architectural and Civil Engineering Institute, 7(1), 88-93, 1991 (in Chinese).

543   Li, H. N., and Sun, L. Y.: Rotational components of earthquake ground motions

544   derived from surface waves, Earthq. Eng. Eng. Vib., 21(1), 15-23,

545   https://link.oversea.cnki.net/doi/10.13197/j.eeev.2001.01.003, 2001 (in Chinese).

546   Li, P. X., Lin, W. J., Zhang, X. M., and Wang, X. M.: Comparisons for regular

547   splitting and non-splitting perfectly matched layer absorbing boundary

548   conditions. Acta Acustica, 40(01), 44-53,

549   https://link.oversea.cnki.net/doi/10.15949/j.cnki.0371-0025.2015.01.006, 2015.

550   Press, W., Flannery, B., Teukolsky, S., and Vetterling, W.: Numerical recipes: The art

551   of scientific computing, Cambridge University Press, 1986.

552   Régnier, J., Bonilla, L. F., Bard, P. Y., et al.: PRENOLIN: International benchmark

553   on 1D nonlinear site-response analysis—Validation phase exercise. Bull.

554   Seismol. Soc. Am., 108(2), 876-900. https://doi.org/10.1785/0120170210, 2018.

555   Renaud, G., Le Bas, P. Y., and Johnson, P. A.: Revealing highly complex elastic

556   nonlinear (anelastic) behavior of Earth materials applying a new probe: Dynamic

557   acoustoelastic testing, J. Geophys. Res.-Solid Earth, 117, B06202,

558   https://doi.org/10.1029/2011JB009127, 2012.

Renaud, G., Rivière, J., Le Bas, P. Y., and Johnson, P. A.: Hysteretic nonlinear elasticity of Berea sandstone at low-vibrational strain revealed by dynamic acoustoelastic testing, Geophys. Res. Lett., 40(4), 715-719, https://doi.org/10.1002/grl.50150, 2013.

Stockwell, R. G., Mansinha, L., and Lowe, R. P.: Localization of the complex spectrum: the S transform, IEEE Transactions on Signal Processing, 44(4), 998-1001, https://doi.org/10.1109/78.492555. 1996.

Sun, L., Yu, Y., Lin, J. Q., and Liu, J. L.: Study on seismic rotation effect of simply supported skew girder bridge, Earthquake Engineering and Engineering Dynamics, 37(4), 121-128, https://doi.org/10.13197/j.eeev.2017.04.121.sunl.014, 2017 (in Chinese).

Sun, L. X., Zhang, Z., and Wang, Y.: Six-component elastic-wave simulation and analysis, EGU General Assembly 2018, Geophysical Research Abstracts, 20, EGU2018-14930-1, 2018.

TenCate, J. A., Malcolm, A. E., Feng, X., and Fehler, M. C.: The effect of crack orientation on the nonlinear interaction of a P wave with an S wave, Geophys. Res. Lett., 43(12), 6146-6152, https://doi.org/10.1002/2016GL069219, 2016.

Tromp, J., and Trampert, J.: Effects of induced stress on seismic forward modelling and inversion. Geophys. J. Int., 213(2), 851-867. https://doi.org/10.1093/gji/ggy020, 2018.

Virieux, J.: P-SV wave propagation in heterogeneous media; velocity-stress finite-difference method, Geophysics, 51(4), 889-901,

581   https://doi.org/10.1190/1.1442147, 1986.

582   Xu, Y. X., Xia, J. H., and Miller, R. D.: Numerical investigation of implementation of

583   airearth boundary by acoustic-elastic boundary approach, Geophysics, 72 (5),

584   SM147–SM153, https://doi.org/10.1190/1.2753831, 2007.

585   Yan, Y. Y.: Seismic response analysis of high-rise building under different types of

586   multi-dimensional earthquake ground motions (Ph.D. dissertation), Jiangsu

587   University, 2017(in Chinese).

588   Zhou, C., Zeng, X. Z., Wang, Q. L., Liu, W. Y., and Wang, C. Z.: Rotational motions

589   of the Ms7.0 Jiuzhaigou earthquake with ground tilt data, Science China Earth

590   Science, 62(5), 832-842, https://doi.org/10.1007/s11430-018-9320-3, 2019.